Supplementary material for: "Ellipsoidal drop impact on a solid surface for rebound suppression"

SUNGCHAN YUN AND GEUNBAE LIM

Department of Mechanical Engineering, Pohang University of Science and Technology (POSTECH), San 31, Hyoja-dong, Pohang, 790-784, Republic of Korea

In this supplementary material, we investigate the effect of the oscillating phase on the impact dynamics and the rebound suppression (section S1). We discuss the validation of the numerical model (section S2). We describe details of scaling models for the maximal extension as a function of AR and We (section S3). We investigate the axis-switching time as a function of AR and We (section S4). We supplement a nonaxial distribution of kinetic energy at the axis-switching time (section S5). Lastly, we investigate nonaxisymmetrical retraction dynamics (section S6).

S1. The role of the oscillating phase on the impact

S1.1. The effect of the oscillating phase on the rebound suppression

The impact behavior and the rebound suppression depends strongly on the aspect ratio of drops just before impact. In figure S1, the drop was impacting with nearly axisymmetric shape ($AR \sim 1.10$), resulting in rebound; By contrast, nonaxisymmetric drops ($AR \sim$ 1.62 or 0.61) obtained by adjusting the falling height resulted in rebound suppression. The AR represents a ratio of the diameter of the x-axis to that of the y-axis, thus $AR = D_x/D_y$.

S1.2. The effect of the oscillating phase on the impact dynamics: contracting drop and expanding drop just before impact

We investigated a difference between the impact of a drop that is overall trying to expand and the same experiment done with a drop that is trying to contract just before impact (figure S2(a)). We had two drops with the same aspect ratio and impact velocity ($We \sim 33$) before impact. Figure S2(b) shows the almost same spreading and retraction behaviors between expanding and contracting drops. Accordingly, we found that the impact behavior is weakly dependent on the drop oscillation at $We \sim 33$.

We can also realize the effect of the oscillation on the impact behavior by simply estimating the ratio of the oscillating time scale ($\sim (\rho D_0^3/\sigma)^{1/2}$) to the crashing time scale ($\sim D_0/U_0$). The ratio of the time scales is proportional to $We^{1/2}$, thus implying that the drop oscillation only slightly affects the impact behavior at high We because the shortest time is dominant.

S1.3. Comparison of the impact dynamics between oblate and prolate shape

We investigated the similarity of the impact behavior between oblate and prolate shape at the same AR by using the simulation. Once ARs are identical, the impact behavior of the oblate drop is only slightly different from that of the prolate drop as shown in figure S3.

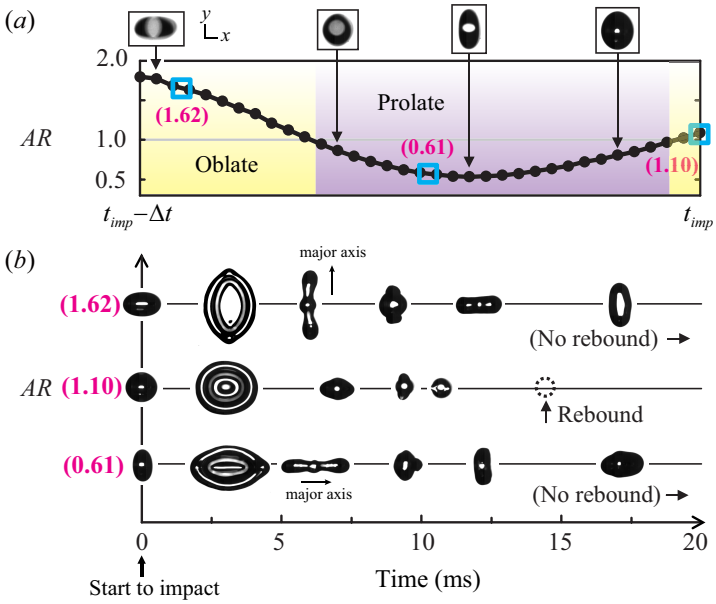

FIGURE S1. (Color online) (a) Variation of the aspect ratio of drops just before impacting at $t = t_{imp}$; $We = 33$ and $\Delta t = 7$ ms. (b) Impacting behaviors depending on AR at the moment of impact; the ARs are equal to 1.62, 1.10, and 0.61, which are also shown in (a). All drops were viewed from the bottom (xy-plane), while focused on solid surfaces. The AR represents a ratio of the diameter of the x-axis to that of the y-axis, thus $AR = D_x/D_y$.

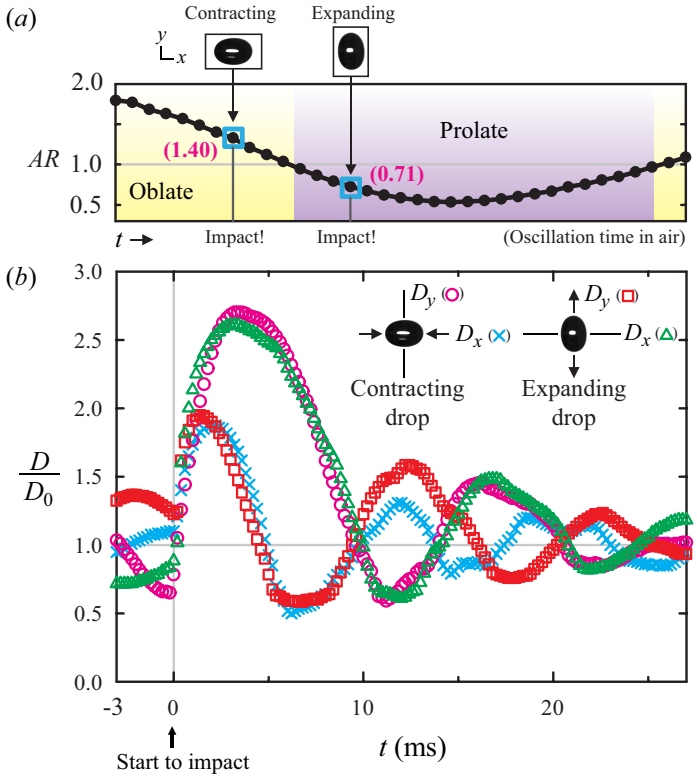

FIGURE S2. (Color online) (a) Aspect ratios of oscillating drops in air. (b) Time evolutions of the contracting drop and the expanding drop; in two cases, the Weber number is equal to 33, and ARs ($= D_x/D_y$) are equal to 1.40 for oblate and 0.71 ($\sim 1.40^{-1}$) for prolate.

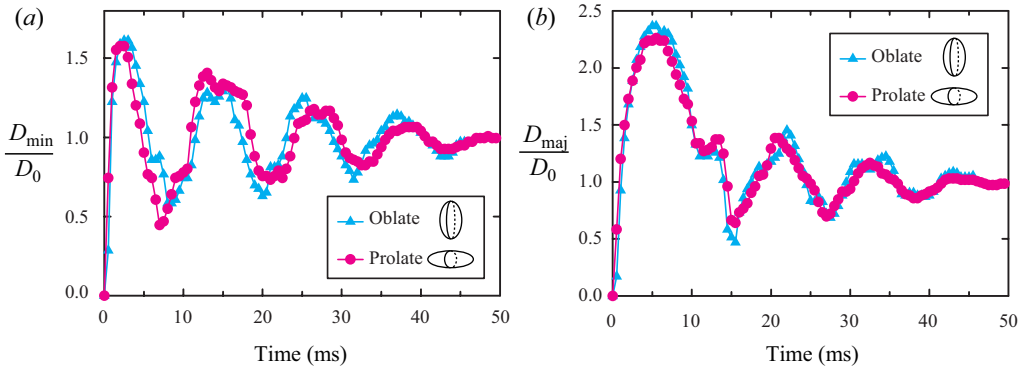

FIGURE S3. (Color online) Comparison of the diameters of (a) the minor axis and (b) the major axis, obtained by the simulation; the major axis denotes the longitudinal direction of the first liquid alignment during retraction, as indicated in figure S1(b). The Weber number is equal to 18, and ARs are equal to 1.65 for oblate and 1.63 for prolate.

S2. Numerical model validation

In figure 8(b), the rebound/deposition transition curve obtained from the simulation slightly shifted to the right, with respect to that obtained from the experiment. A possible reason to account for this discrepancy could be the complicated contact angle dynamics induced by contact angle hysteresis and contact line friction, which have not been considered in the simulation. Using the tilting base method (Extrand & Kumagai 1997), the contact angle hysteresis we measured was $10 \pm 3^\circ$ on the Teflon-coated surface. We also measured dynamic contact angles in the drop impact experiment for the principal axes (figure S4). We tried to represent the dynamics economically by using the adequate contact angle ($\theta = 100^\circ$) that can approximately reproduce the experimental data of the temporally resolved contact diameters for the horizontal axes (figure S5), which is similar to the previous work (Gunjal *et al.* 2005). Our model reasonably predicted the contact diameters for all the ARs as shown in figure S6. The maximal extension during spreading could be predicted within an accuracy of 5% (figure S7). However, the model is not responsible for the temporal variation of the height (a distance from the solid to the apex of the drop), which can be directly related to the rebounding.

Thus, we investigated the temporal variation of the height of drops for the experiment and the simulation at the same AR and We. During retraction, drops elongated vertically and reached the maximal height. We were able to come up with a good prediction as shown in figure S8. However, there was a slight difference between the experiment and the simulation: the maximal height of the simulation was typically higher than that of the experiment. We have shown that a more elongated liquid column causes lower degree of the axis switching because of weaker amplitudes of the horizontal oscillation, which leads to a drop rebound. It means that as the height of the liquid column increases at the same AR (figure S9), there is a high probability of drop rebound. We reason out that the shift of transition curves may be due to the discrepancy of maximal heights.

We attempted to account for the discrepancy of maximal heights between the experiment and the simulation. One possibly minor reason could be an effective interfacial tension induced by an electric charge, which has not also been considered in the simulation. Assuming that the drops get in contact with dielectric substances on impact, we can reason out that drops are at least partially conducting, and the charge moves around the surface. As a consequence, the effective surface tension can spatially vary. An effective interfacial tension is given by $\sigma^e = \sigma_0 - (q/8\pi)^2/(\varepsilon R^3)$ (Davis & Bridges 1994), where σ_0, q, and ε are the interfacial tension of the neutral surface, the amount of charge, and the permittivity of the surrounding medium, respectively. It means a decrease in interfacial tension for charged drops by 0.77 times ($q = 0.30 \pm 0.01$ nC, $\sigma^e = 55$ mN m^{-1}), compared with neutral drops ($\sigma_0 = 72$ mN m^{-1}). Another possible reason could be the inability to accurately predict the complex contact angle dynamics, as mentioned earlier, which plays an important role in changing drop shapes. These reasons are the possible explanations for the discrepancy of the maximal height.

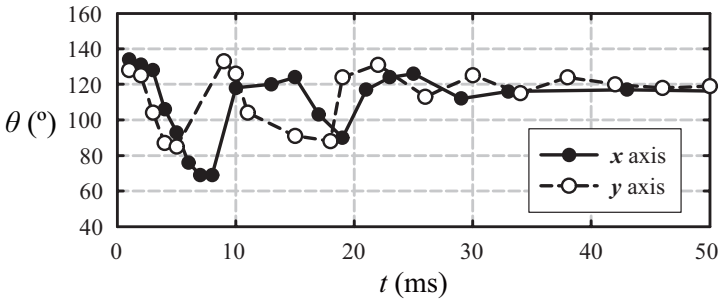

FIGURE S4. (a) Dynamic contact angle of the impacting drop ($AR = 1.43$ and $We = 23$) in the x-axis and the y-axis, obtained experimentally. The drop begins to spread at $t = 0$ ms.

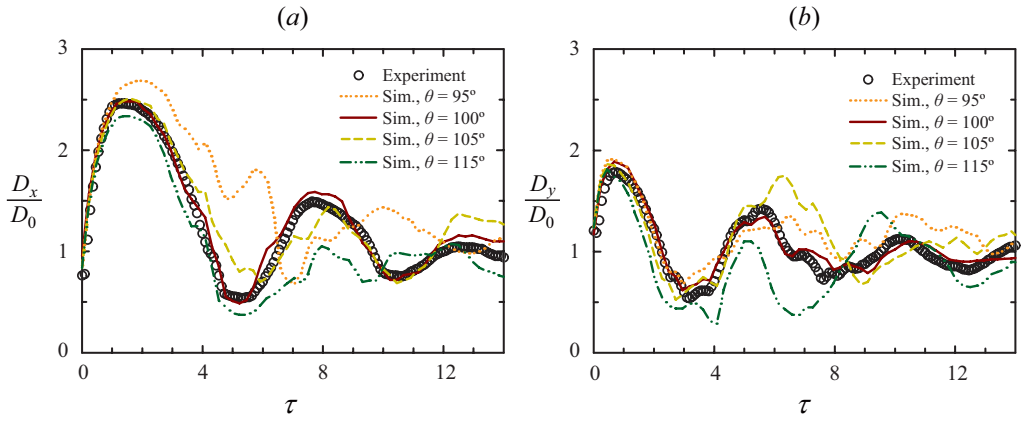

FIGURE S5. (Color online) Validation of the contact angle model used in this work, based on the widths of (a) the x-axis and (b) the y-axis at $AR = 1.63$ and $We = 23$. A contact angle of 100° is suitable to reproduce the impact dynamics observed in the experiment.

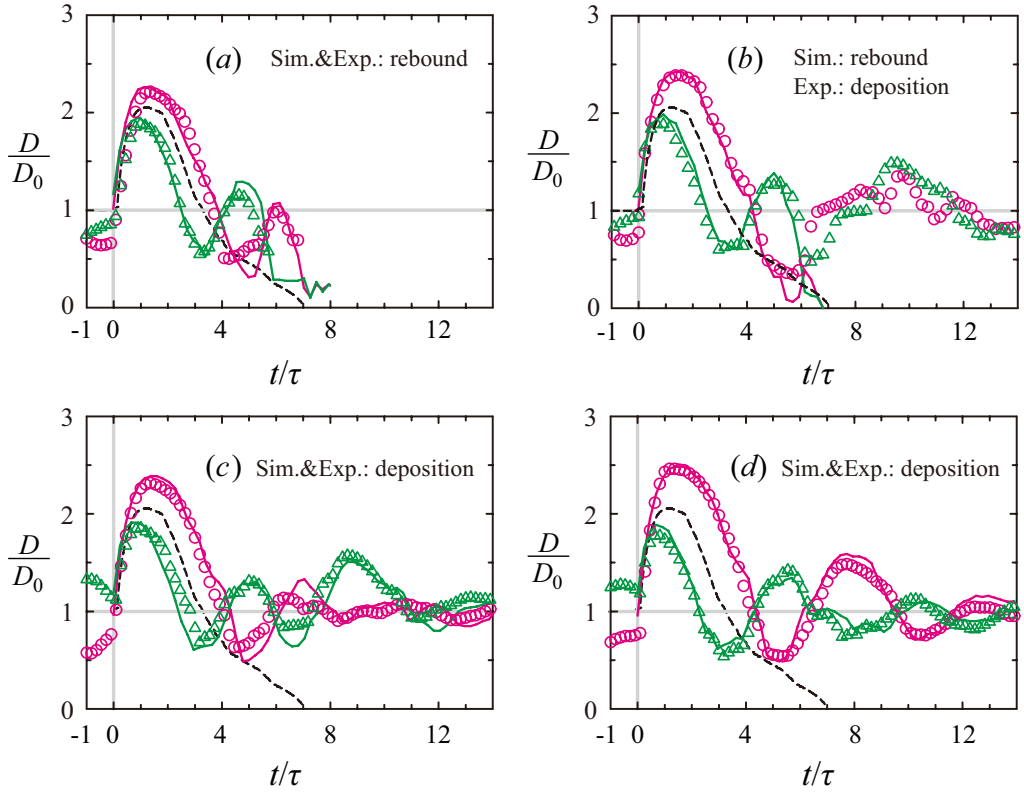

FIGURE S6. (Color online) (a) Temporal evolutions of the normalized contact diameters (D/D_0) of drops with ARs of (a) 1.26 (sim.) and 1.20 (exp.); (b) 1.36 (sim.) and 1.30 (exp.); (c) 1.43 (sim.) and 1.38 (exp.); (d) 1.63 (sim.) and 1.62 (exp.) at the same impact velocity ($We = 23$). The symbols denote the experimental results in the x-axis (◯) and y-axis (△). The solid lines indicate the simulation results in the x-axis (pink line) and y-axis (green line). The dashed lines represent the temporal variations of the diameters of typical drops ($AR = 1.0$) obtained experimentally. The standard deviation of the experimental result is within 7%.

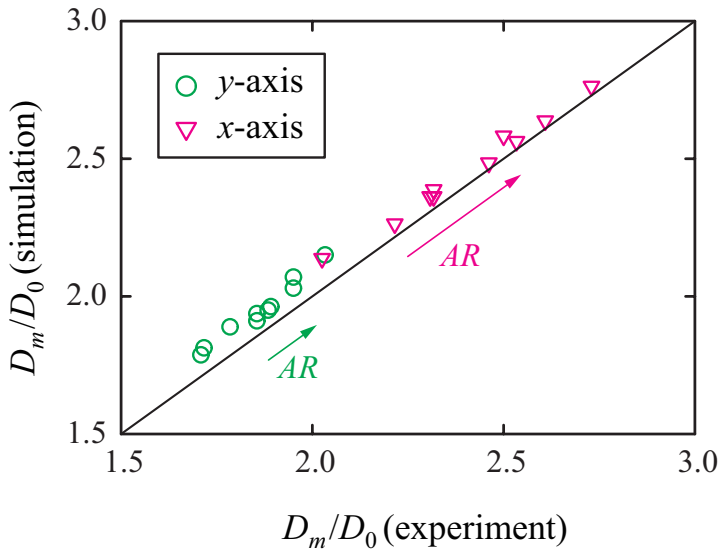

FIGURE S7. (Color online) Comparison of the numerical results with the experimental results, based on maximal extensions of the principal axes for ten different ARs. The model predicts the maximal extension within an accuracy of 5%.

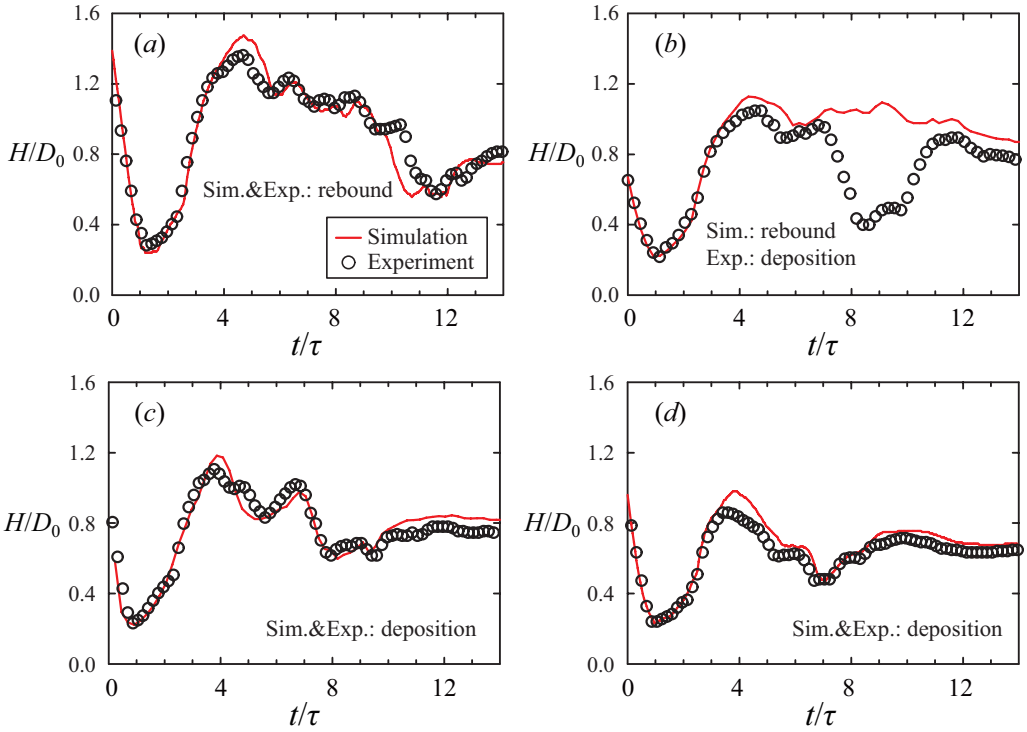

FIGURE S8. (Color online) Temporal evolutions of the normalized height (H/D_0) of drops with ARs of (a) 1.26 (sim.) and 1.20 (exp.); (b) 1.36 (sim.) and 1.30 (exp.); (c) 1.43 (sim.) and 1.38 (exp.); (d) 1.63 (sim.) and 1.62 (exp.) at the same impact velocity ($We = 23$). The normalized height denotes the distance from the bottom plate to the apex of the drop. The standard deviation of the experimental result is within 7%.

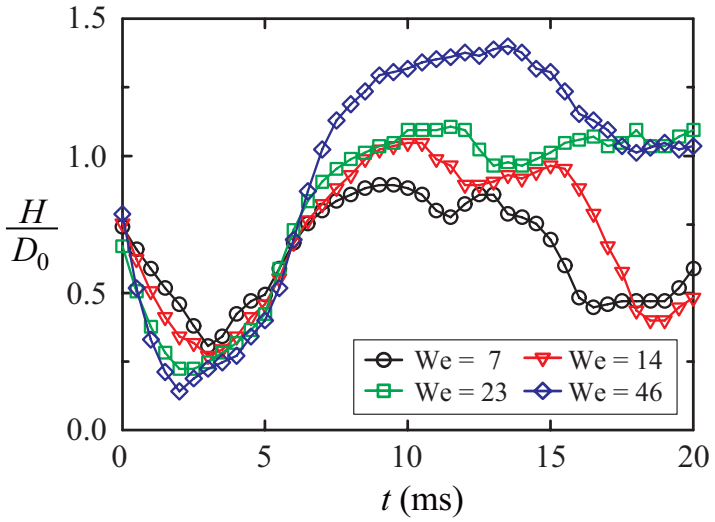

FIGURE S9. (Color online) (*a*) Temporal variations of the normalized heights of drops (H/D_0) from the substrate to the apex, obtained numerically as a function of We at a constant AR of 1.36.

S3. Scaling analysis on the maximal extensions

To estimate the scaling relation of D_{my}, we incorporated an axisymmetric model, wherein drops radially spread with the initial horizontal diameter of b and the initial vertical length of a, and reach the maximal extension in the y-axis, as observed at $t \sim (1/2)\tau$ in figure S10. There would be a mass inequality between the model and the original drop. Thus we introduced an impact velocity V_0 for the model and indicated the corresponding kinetic energy in figure S11. A capillary-inertia balance for the model provides us a relation $\sigma/h^2 \sim \rho V_0^2/a$, which derives $\sigma/h^2 \sim \rho U_0^2/b$ from a consistency of the initial kinetic energy with $V_0^2 = (a/b)U_0^2$, as denoted in figure S11. The resulting relation can be written as $D_{my}/D_0 \sim AR^{-1/6}\,We^{1/4}$, which is consistent with (4.1). The model is valid for the prolate ellipsoid of the original drop. We observed that the experimental data are well-fitted to the scaling relation of D_{my}.

For the scaling relation of D_{mx}, we also assumed that a prolate drop spreads with the initial vertical length of a and reaches the elliptic puddle which has the same D_{my} in the previous step as observed at $t \sim \tau$ in figure S10. We obtained the relation $D_{mx}/D_0 \sim AR^{1/3}\,We^{1/4}$ from a capillary-inertia balance and a volume conservation, which is consistent with (4.2), and observed that the experimental data are also well-fitted to the scaling relation of D_{mx}.

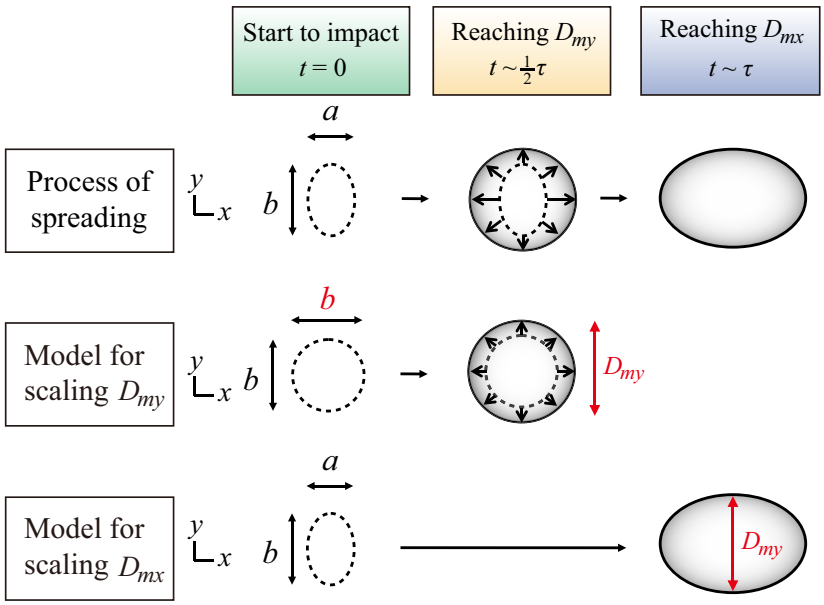

FIGURE S10. (Color online) Schematic of the models for scaling D_{my} and D_{mx}.

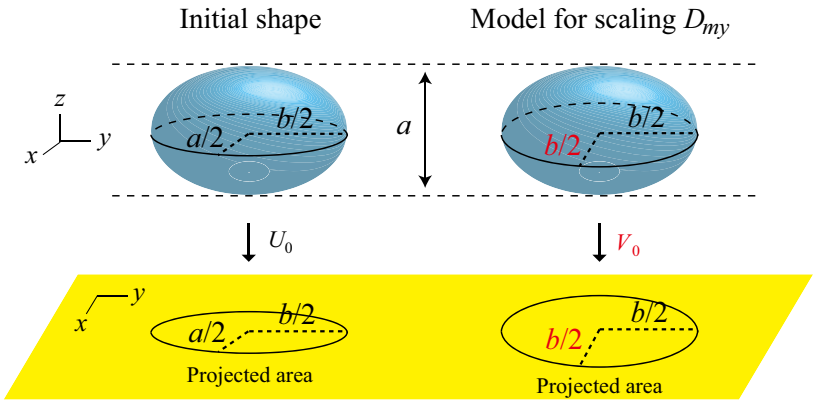

Mass:	$\pi\rho ba^2/6$	$\pi\rho b^2a/6$
Impact velocity:	U_0	V_0
Initial KE:	$\pi\rho ba^2U_0^2/12$	$\pi\rho b^2aV_0^2/12$

FIGURE S11. (Color online) Initial prolate shape at the moment of the impact and the model used for scaling D_{my}.

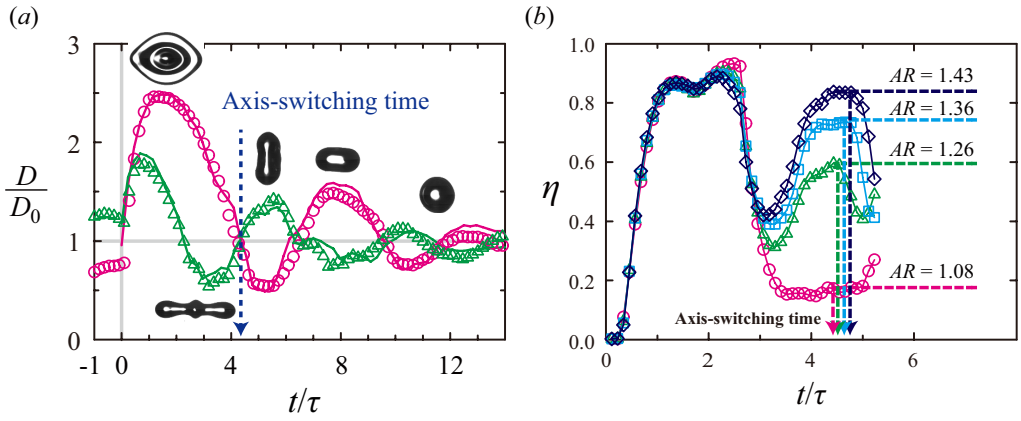

FIGURE S12. (Color online) (a) Axis-switching time (arrow) means the time wherein the contact width of the x-axis intersects with that of the y-axis at $t \sim 4.5\tau$; the plot is the same with figure 4(c). (b) The value of η measured at the axis-switching time (arrows) is defined as a nonaxial distribution of KE at the axis-switching time (η_s); the plot is the same with figure 9(a)

S4. Axis-switching time

We defined the axis-switching time (t_s) wherein the contact width of the x-axis (D_x) intersects with that of the y-axis (D_y) during the first axis switching, as shown at $t \sim 4.5\tau$ in figure S12(a). Based on the axis-switching time of the numerical data (figure S13(a)), we found a relation of $t_s/\tau \sim 0.9AR^{1/4}We^{1/2}$ (figure S13(b)). From the relation, normalized axis-switching times (t_s/τ) can be estimated as 4.40, 4.57, 4.66, and 4.72 with increasing AR, as indicated in figure S12(b).

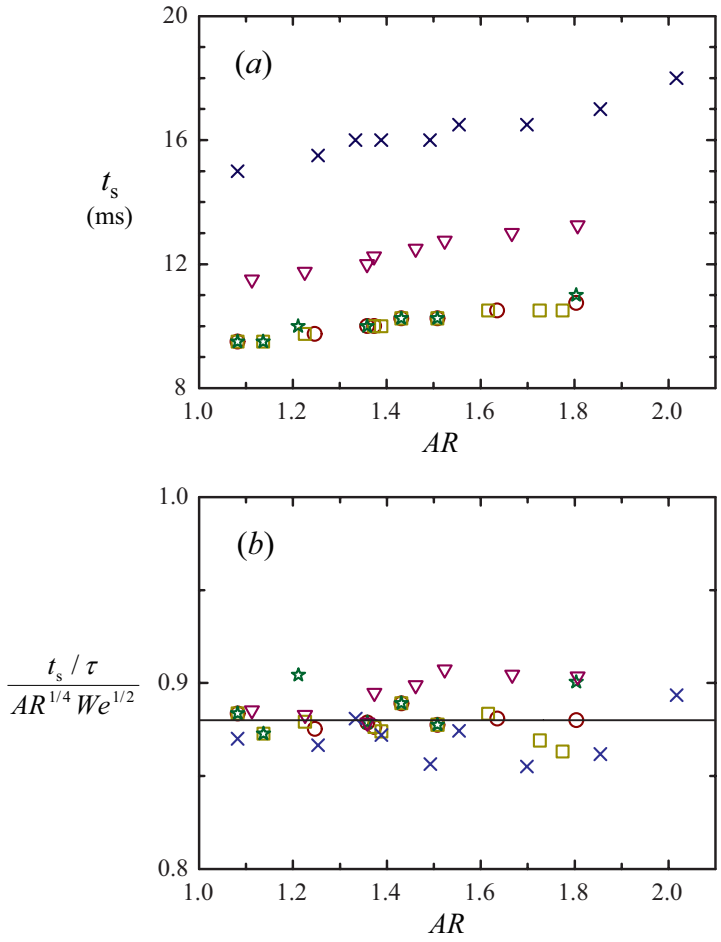

FIGURE S13. (Color online) (a) Axis-switching time (t_s) as a function of AR. All the symbols are described in table S1. (b) The axis-switching time scales as $t_s/\tau \sim 0.9 AR^{1/4} We^{1/2}$, where $\tau = D_0/U_0$.

Symbols in figure S13	Impact velocity, U_0 (m s^{-1})	Surface tension, σ (mN m^{-1})	$We = \rho D_0 U_0^2/\sigma$
□	0.5	72	7
☆	0.7	72	14
×	0.5	28	18
◯	0.9	72	23
▽	0.9	50	32

TABLE S1. Numerical conditions in data of figure S13 and the corresponding Weber number

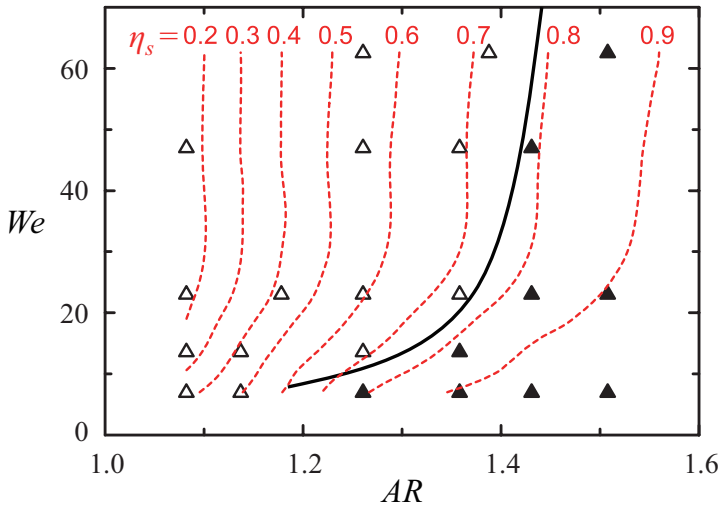

FIGURE S14. (Color online) Rebound/deposition transition (solid line) and contour lines of η_s (dashed line) for the contact angle model of 100°. The η_s denotes the value of measured at the axis-switching time.

S5. Nonaxial distribution of kinetic energy (η) associated with the rebound/deposition transition

We defined η_s as the value of η measured at the axis-switching time. Our numerical study showed that the critical value of η_s can be a crucial factor in representing the actual rebound/deposition transition curves. In other words, the η_s determines the outcome of the impact. To demonstrate this finding, we plotted contour lines of η_s with the transition curve as a function of AR and We in figure S14 (open symbol: rebound; filled symbol: deposition). The rebound and deposition regimes can be separated using the critical value of $\eta_s = 0.77$, indicating that the rebound can be suppressed when the nonaxial kinetic energy (KE) is higher than 77% of the total KE at the axis-switching time. We further investigated the transition curves and contour lines of η_s by varying the surface wettability. The rebound and deposition regimes can be separated by values of η_s between 0.7 and 0.8, as shown in figure S15. From the actual transition curves and the equi-value lines of $\eta_s = 0.77$ in figure S16, we are convinced that the η_s is fairly related to the outcome of the impact.

We briefly discussed the rebound/deposition transition curve in the view point of the η_s. First, we considered the case where AR is varied at the constant We. An increasing AR induces the high η_s and the consequent massive kinetic energy transfer between the horizontal principal axes (x and y) rather than the vertical axis (z), thereby leading to rebound suppression (Yun *et al.* 2013). Secondly, we considered the case where We is varied at the constant AR. During retraction, drops elongate vertically with the formation of the liquid column as We increases (§ S2). The axis switching rarely develops in the liquid column because it weakens the horizontal surface oscillation, consequently reducing the kinetic energy transfer between the horizontal principal axes. Accordingly, the higher the We, the weaker the η_s, which may cause the drop rebound. However, η_s becomes invariant when We is more than 40, as shown in figure 9(b). Therefore, we expect that the rebound/deposition transition can be determined mainly by AR at high We.

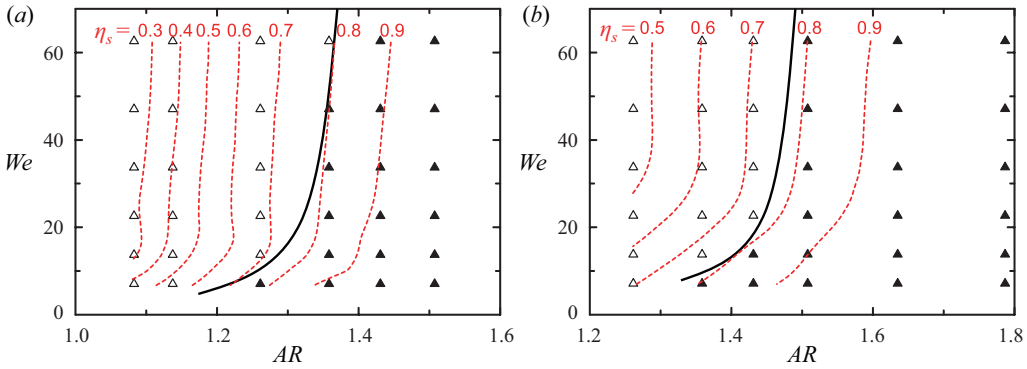

FIGURE S15. (Color online) Rebound/deposition transition (solid line) and contour lines of η_s (dashed line) for contact angle models of (a) 95° and (b) 105°.

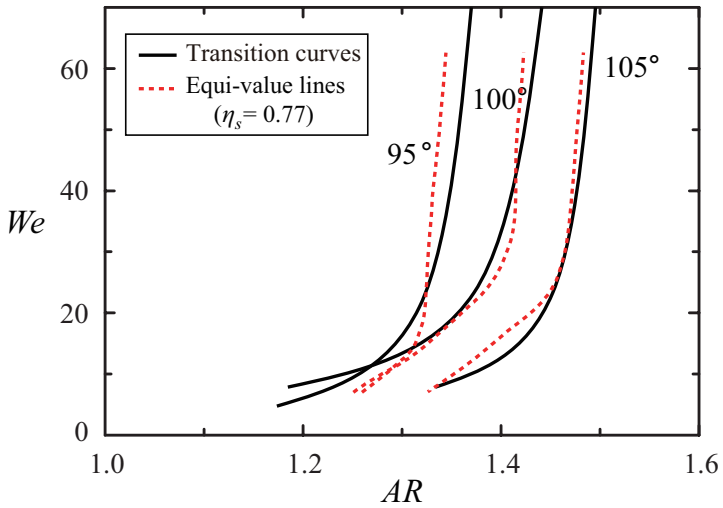

FIGURE S16. (Color online) Comparison between the transition curves and equi-value lines of $\eta_s = 0.77$ for different contact angle models.

S6. Nonaxisymmetrical retraction dynamics

We observed that the nonaxial distribution of KE at the axis-switching time (η_s) depends on We. We associate its dependence on the We with the retracting process rather than the spreading process because the ratio of maximal extensions is found to be independent of the We, following the scaling relation, $D_{mx}/D_{my} \sim AR^{1/2}$. To quantify the retracting behaviors, we plotted in figure S17(a) temporally resolved widths of the x-axis (dotted line) and y-axis (solid line) obtained numerically for varying We and the constant AR of 1.36. The widths of the two axes have a tendency to intersect at the first axis-switching time $t \sim 9$ ms. After the retraction along the x-axis finishes at $t \sim 11$ ms, the rebound is suppressed for $We = 7$ and 14, whereas not suppressed for $We = 23$ and 46. Note that the Weber numbers were obtained by varying the impact velocity. When in general drops impact at the low viscosity regime, a retraction velocity is represented as $V_{ret} \sim (\sigma/\rho\delta)^{1/2}$ where δ is the film thickness (Thoroddsen *et al.* 2003; Bartolo *et al.* 2005; Eggers *et al.* 2010). By using volume conservation, δ approximates to $D_0^3 D_m^{-2}$, which introduces a retraction rate ($\dot{\epsilon} \equiv V_{ret}/D_m$). It can be written considering the effect of surface wettability (Bartolo *et al.* 2005) as

$$\dot{\epsilon} \sim (\frac{2}{3}\rho D_0^3/\sigma)^{-1/2}(1-\cos\theta_R)^{1/2}. \tag{1}$$

The equation indicates that the retraction rate is independent of impact velocity. For a nonaxisymmetrical drop impact, however, we found not only a notable difference of the retraction rate between two principal axes but also its dependence on the impact velocity. When the widths of two axes are normalized by each maximal extension, the retraction rates ($\dot{\epsilon}$) can be represented by the slopes of the curves marked by short straight lines, as shown in figure S17(b). All the cases of the y-axis collapsed onto a single curve until $t \sim 6$ ms, showing $\dot{\epsilon}_y \sim 150$ s^{-1}, which means that the retraction rate in the y-axis is independent of We. The rate is comparable to the predicted retraction rate, $\dot{\epsilon} \sim 130$ s^{-1}, obtained from (1). By contrast, retraction rates in the x-axis are found to be $\dot{\epsilon}_x \sim 25$, 59, 94, and 98 s^{-1} with increasing We.

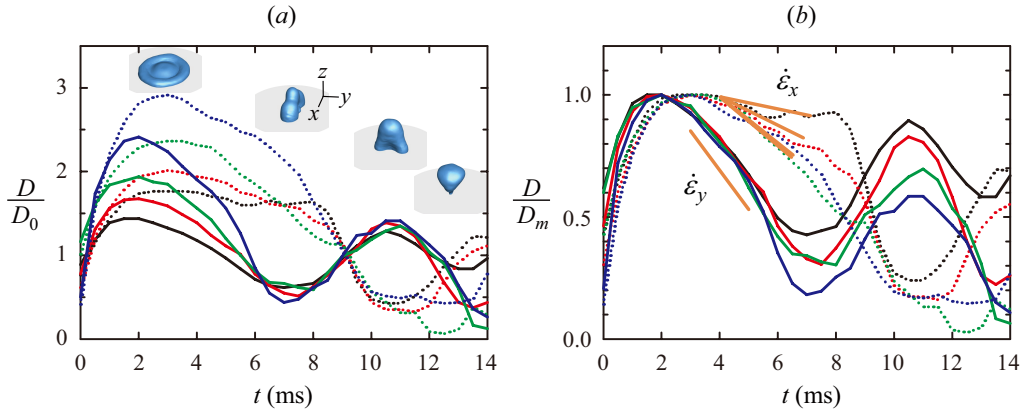

FIGURE S17. (Color online) (*a*) Temporal variations of widths of the x-axis (dotted line) and y-axis (solid line) obtained numerically for the constant AR of 1.36 and different Weber numbers of 7 (black), 14 (red), 23 (green), and 46 (blue). The rebound is suppressed for $We = 7$ and 14, while not suppressed for $We = 23$ and 46. Images of insets represent impact behaviors for $We = 23$. (*b*) The width of (*a*) is normalized by its maximal extension for each axis. Slopes of the normalized widths represent retraction rates, which are marked by short straight lines (orange). The slopes indicate that $\dot{\epsilon}_x \sim 25$, 59, 94, and 98 s^{-1} with increasing We, and that $\dot{\epsilon}_y \sim 150$ s^{-1} independent of We.

REFERENCES

EXTRAND, C. W. & KUMAGAI, Y. 1997 An experimental study of contact angle hysteresis. *J. Colloid Interface Sci.* **192**, 378–383.

DAVIS, E. J. & BRIDGES, M. A. 1994 The Rayleigh limit of charge revisited: light scattering from exploding droplets. *J. Aerosol Sci.* **25**, 1179–1199.

GUNJAL, P. R., RANADE, V. V. & CHAUDHARI, R. V. 2005 Dynamics of drop impact on solid surface: Experiments and VOF simulations. *AICHE J.* **51**, 59–78.

THORODDSEN, S. T., ETOH, T. G. & TAKEHARA, K. 2003 Air entrapment under an impacting drop. *J. Fluid Mech.* **478**, 125–134.

BARTOLO, D., JOSSERAND, C. & BONN, D. 2005 Retraction dynamics of aquous drops upon impact on nonwetting surfaces. *J. Fluid Mech.* **545**, 329–338.

EGGERS, J., FONTELOS, M. A., JOSSERAND, C. & ZALESKI, S. 2010 Drop dynamics after impact on a solid wall: Theory and simulations. *Phys. Fluids* **22**, 062101.

YUN, S., HONG, J. & KANG, K. H. 2013 Suppressing drop rebound by electrically driven shape distortion. *Phys. Rev. E* **87**, 033010.